

A hybrid scheme coupling lattice Boltzmann method and finite-volume lattice Boltzmann method for steady incompressible flows

Cite as: Phys. Fluids **34**, 037114 (2022); <https://doi.org/10.1063/5.0085370>

Submitted: 15 January 2022 • Accepted: 06 March 2022 • Published Online: 23 March 2022

Mengke Wen (温梦珂),  Weidong Li (李维东) and Zhangyan Zhao (赵章焰)

COLLECTIONS

Paper published as part of the special topic on [Special Issue on the Lattice Boltzmann Method](#)



[View Online](#)



[Export Citation](#)



[CrossMark](#)

ARTICLES YOU MAY BE INTERESTED IN

[High-order methods for diffuse-interface models in compressible multi-medium flows: A review](#)

[Physics of Fluids](#) **34**, 021301 (2022); <https://doi.org/10.1063/5.0077314>

[Modeling of three-phase displacement in three-dimensional irregular geometries using a lattice Boltzmann method](#)

[Physics of Fluids](#) **33**, 122108 (2021); <https://doi.org/10.1063/5.0068759>

[Effect of the odd and even number of blades on the hydrodynamic performance of a pre-swirl pumpjet propulsor](#)

[Physics of Fluids](#) **34**, 035120 (2022); <https://doi.org/10.1063/5.0080661>

APL Machine Learning

Open, quality research for the networking communities

Now Open for Submissions

[LEARN MORE](#)

A hybrid scheme coupling lattice Boltzmann method and finite-volume lattice Boltzmann method for steady incompressible flows

Cite as: Phys. Fluids 34, 037114 (2022); doi: 10.1063/5.0085370

Submitted: 15 January 2022 · Accepted: 6 March 2022 ·

Published Online: 23 March 2022



View Online



Export Citation



CrossMark

Mengke Wen (温梦珂),¹ Weidong Li (李维东),^{1,2,a)} and Zhangyan Zhao (赵章焰)^{1,a)}

AFFILIATIONS

¹School of Transportation and Logistics Engineering, Wuhan University of Technology, Wuhan 430070, China

²Hypervelocity Aerodynamics Institute, China Aerodynamics Research and Development Center, P.O. Box 211, Mianyang 621000, China

Note: This paper is part of the Special Issue on the Lattice Boltzmann Method.

^{a)}Authors to whom correspondence should be addressed: lwd_1982.4.8@163.com and 13871001982@163.com

ABSTRACT

We present a new hybrid method coupling the adaptive mesh refinement lattice Boltzmann method (AMRLBM) and the finite-volume lattice Boltzmann method (FVLBM) to improve both the simulation efficiency and adaptivity for steady incompressible flows with complex geometries. The present method makes use of the domain decomposition, in which the FVLBM sub-domain is applied to the region adjacent to the walls, and is coupled to the lattice Boltzmann method (LBM) sub-domain in the rest of the flow field to enhance the ability of the LBM to deal with irregular geometries without sacrificing the high efficiency and accuracy property of the LBM. In the LBM sub-domain, a cell-centered lattice structure-based AMRLBM is used and, in the FVLBM sub-domain, the gas-kinetic Bhatnagar–Gross–Krook (BGK) scheme-based FVLBM is adopted to reduce the numerical dissipation and enhance the efficiency of FVLBM. Moreover, not like the conventional LBM and Navier–Stokes equation solver-based hybrid schemes, the present hybrid scheme combines two kinds of lattice Boltzmann equation solvers, that is, AMRLBM and FVLBM, which makes the present scheme much simpler and better consistency than the conventional hybrid schemes. To assess the accuracy and efficacy of the proposed method, various benchmark studies, including the Kovasznay flow, the lid-driven cavity flow with Reynolds number $Re = 100, 400$, and 1000 , and the steady flow past a cylinder with $Re = 20$ and 40 , are also conducted. The numerical results show that the present scheme can be an efficient and reliable method for steady incompressible flows.

Published under an exclusive license by AIP Publishing. <https://doi.org/10.1063/5.0085370>

I. INTRODUCTION

Over the last two decades, the lattice Boltzmann method (LBM) has been validated as an effective computational fluid dynamics (CFD) tool for tackling the numerical simulation of the nearly incompressible flow problem. Nevertheless, due to the closely coupled discretizations of phase space and time,^{1,2} the LBM is associated with the uniform Cartesian meshes, which exists as a great impediment in simulating flows involving complicated geometries, such as curve boundaries, inclined walls, and so on. To circumvent the restriction of uniform Cartesian meshes, the lattice Boltzmann schemes with the adaptive mesh refinement (AMR), the off-lattice Boltzmann methods, and the hybrid lattice Boltzmann methods have been developed. In the AMR method,^{3–5} the mesh refinement was employed in those regions of the computation domain where a high resolution is needed. With the flexibility of the refinement techniques on mesh resolution, the AMR

lattice Boltzmann method (AMRLBM) greatly improves the adaptivity on complex geometries, but it approximates the curve boundaries with steps, which can not exactly represent the irregular boundary geometries. As for the off-lattice Boltzmann methods, including the finite difference lattice Boltzmann method (FDLBM),^{6,7} the finite-volume lattice Boltzmann method (FVLBM),^{8–10} the spectral difference lattice Boltzmann method,^{11,12} and so on, since the body-fitted meshes can be used, these methods overcome the inability of the LBM to simulate flows with irregular boundaries. As one of these off-lattice Boltzmann methods, the FVLBM^{9,13–16} was receiving more and more attention due to its robustness and flexible use of unstructured meshes to handle irregular geometries and has been established as an accurate approach to simulate incompressible flows. However, compared with the LBM, the FVLBM generally has relatively low efficiency.¹⁷ Alternatively, to combine the high efficiency of mesoscopic LBM and the good

adaptivity on complex geometries of the methods including finite difference method (FDM), finite-volume method (FVM), a number of hybrid lattice Boltzmann method (HLBM) have been developed to simulate various complicated fluid problems, such as the multiscale thermal problems,^{18,19} the multi-scale multi-physicochemical processes,²⁰ the pore-scale simulations of porous media,^{21,22} the fouling processes,^{23,24} the fluid-structure interaction problems,²⁵ the high-Re flows,²⁶ and so on. In general, for these complicated flows, only one kind of method, that is, LBM or FDM/FVM, cannot obtain the best efficiency and accuracy.

The existing work on the HLBMs can be divided into two categories. The first category of these hybrid lattice methods^{18–22,27–31} generally couples the mesoscopic LBM and the macroscopic Navier–Stokes equation (NS) solver, that is, FDM or FVM for NS. In this kind of hybrid method, the computational domain is decomposed into lattice Boltzmann equation (LBE) region and the NS region in which the flow-field is solved by LBM and macroscopic NS solver, respectively. The numerical results in different sub-domains are coupled at their interfaces. As for the hybrid scheme coupling LBM and FDM (hybrid LBM-FDM), in 2004, Albuquerque *et al.*²⁷ discussed how a lattice Boltzmann (LB) scheme can be spatially coupled with a finite difference (FD) scheme and proposed a hybrid LBM and FDM scheme in which the coupling methodology of the LB distribution functions and the macroscopic physical quantities were obtained by the Chapman–Enskog expansion of the lattice Boltzmann equation. To simulate unsteady problems, Astorino *et al.*²⁹ extended the hybrid LBM-FDM to time-dependent problems with the Parareal paradigm to couple the LBM and FDM, where the independent grid size and time step size were allowed. However, the FDM has limitations in handling the problem with very complex computational domains,³² which restricts the development of the hybrid LBM-FDM. Compared with the FDM, FVM has better adaptivity on flows involving irregular geometries, and therefore, the hybrid method coupling LBM and FVM (hybrid LBM-FVM) received much more attention than the hybrid LBM-FDM. In 2010, Luan *et al.*²⁸ developed a hybrid LBM-FVM and reconstruction operators (ROs) for the information exchange of distribution functions and macro variables around the domain interfaces. In this hybrid LBM-FVM, with the ROs in the domain interfaces, the distribution functions of the LBM can be rebuilt by the macroscopic variables in the FVM sub-domain and the macroscopic variables of the FVM can be obtained by taking moments of the distribution functions in the LBM sub-domain, respectively. Then, the general ROs for hybrid LBM-FVM were extended to the numerical simulation of the natural convection problem.¹⁸ To simplify the ROs, Li *et al.*³⁰ proposed another hybrid LBM-FVM to simulate the natural convection, where the non-equilibrium extrapolation method³³ was applied to transfer the information between the macroscopic variables in the FVM region and the mesoscopic distribution functions in the LBM region. To enhance the robustness of the hybrid LBM-FVM, Salimi *et al.*²¹ developed a different hybrid scheme coupling the multiple relaxation time (MRT) and the FVM to simulate flow around the porous obstacle in which a new ROs was provided and the second-order derivatives of the equilibrium distribution functions were considered in this ROs. In 2017, Tong *et al.*³¹ derived different ROs based on the first- and second-order Chapman–Enskog expansions and evaluated the precisions of different ROs with numerical experiments. Moreover, in 2018, Sun *et al.*¹⁹ implemented a hybrid LBM-FVM to

solve the combined conduction–radiation heat transfer problems in irregular geometry. Despite the first category of HLBMs enhancing the geometrical flexibility of the LBM, these methods were based on the LBM and NS solvers, and therefore, the complicated ROs for the information exchange between LBM and NS sub-domains are generally necessary and may not guarantee the momentum conservation.³¹

Similarly, as in the first category of HLBMs, the computational domain in the second category of HLBMs is decomposed into the LBM sub-domain and the FVLBM sub-domain in which the flow-fields are solved by LBM and FVLBM, respectively. However, not as the first category methods, this kind of HLBMs solves the LBE on the whole computational domain, which avoids the complicated distribution function reconstruction from macro variables during the information exchange procedure of the LBM and the macroscopic NS solver in the first category of HLBMs. In 2017, Di Ilio *et al.*³⁴ provided a HLBMs on an overlapping grid system combining the standard LBM and the unstructured FVLBM. In this hybrid method, the information exchange between LBM and FVLBM sub-domains was fulfilled through interpolation in the overlapped region between the LBM and the FVLBM sub-domains. Moreover, in Di Ilio's HLBMs, the FVLBM is an explicit scheme and the time step of the FVLBM is limited by both the Courant–Friedrichs–Lowy (CFL) condition and the relaxation time τ . Therefore, Di Ilio's HLBMs³⁴ has very low efficiency for high Reynolds number flows, where τ can be extremely small. To improve efficiency, Horstmann and coworkers³⁵ developed another HLBMs. Not as Di Ilio's HLBMs, Horstmann's HLBMs adopted a semi-implicit finite-volume formulation, which removes the limitation that the time step should be less than τ . Horstmann's HLBMs can be more efficient than Di Ilio's HLBMs for high Reynolds number flows. However, in Horstmann's HLBMs, a node-based LBM and a structured cell-centered finite-volume method were adopted. As a consequence, an overlapping interface containing at least two grid cells between the LBM and the FVLBM sub-domains should be used in this HLBMs, and therefore, interpolations for obtaining distributions between different sub-domains in the overlapped region cannot be avoided.

To avoid using over-lapped grids and complicated interpolations to exchange distribution functions between LBM and FVLBM, we propose a new HLBMs that couples the AMRLBM⁵ and the FVLBM⁹ without using overlapped grids for steady flows in this work. In the present scheme, there is no overlapped region between the FVLBM and LBM sub-domains. Moreover, the FVLBM proposed by Li and Li⁹ is adopted to solve the flow field of the FVLBM domain, which generally contains the complex boundary geometries. By using the formal analytical solutions of the LBE to determine the fluxes on cell interfaces, which includes the effects of collision terms and is also a function of space and time, Li's FVLBM has low numerical dissipation and achieves second-order spatial-temporal accuracy in one time step. Moreover, this FVLBM is semi-implicit, and therefore, the time step is not limited by τ . Furthermore, in the LBM domain of the proposed HLBMs, a cell-centered block-structured AMR routine⁵ is adopted to simulate the flow field. Thanks to non-overlapping interfaces between the sub-domains, information exchange of distribution functions between the two-side cells can be very straightforward by a ghost cell method without complicated interpolations.

The remainder of this paper is organized as follows. Section II discusses the formulation of the hybrid scheme in detail. Section III introduces the implementations of the AMR routine. Section IV

provides three two-dimensional test cases to validate the proposed hybrid method: (a) the Kovasznay flow with Reynolds number $\text{Re} = 40$; (b) the lid-driven cavity flow with $\text{Re} = 100, 400$, and 1000 ; and (c) the steady flow past a cylinder with $\text{Re} = 20$ and 40 . Finally, Sec. V concludes the paper.

II. NUMERICAL FORMULAS OF THE HYBRID METHOD

In the present hybrid method, the flow field is decomposed into FVLBM domain and the AMRLBM domain. The FVLBM domain comprises the inner part of flow field, which generally contains the physical boundaries with complex geometries, for example, curve walls, inclined walls, and so on, while the AMRLBM domain covers the rest domain of the flow field. The present hybrid scheme couples the AMRLBM and the FVLBM, and makes full use of the advantages of both the LBM and the FVLBM. It enhances the ability of the LBM to deal with irregular geometries by the FVLBM and does not lose the high efficiency and accuracy of the LBM too much. In this section, the numerical description of the AMRLBM and the FVLBM is introduced briefly. Both of these methods solve the same lattice Boltzmann Bhatnagar–Gross–Krook (BGK) model, which reads

$$\partial_t f_\alpha + \xi_\alpha \cdot \nabla_x f_\alpha = \Omega_\alpha \equiv -\frac{f_\alpha - f_\alpha^{eq}}{\tau}, \quad \alpha = 0, \dots, q-1, \quad (1)$$

where $f_\alpha = f_\alpha(\mathbf{x}, \xi_\alpha, t)$ is the distribution functions with the microscopic particle velocity ξ_α at position \mathbf{x} and time t , f_α^{eq} and Ω_α are the equilibrium state and associated collision term with respect to f_α , $\tau = \nu/C_s^2$ is the relaxation time determined by the viscosity coefficient ν and the sound speed $C_s = 1/\sqrt{3}$, and q is the number of discrete velocities. The equilibrium distribution function is given as the following:

$$f_\alpha^{eq} = \omega_\alpha \rho \left[1 + \frac{\xi_\alpha \cdot \mathbf{u}}{C_s^2} + \frac{(\xi_\alpha \cdot \mathbf{u})^2}{2C_s^4} - \frac{\mathbf{u}^2}{2C_s^2} \right], \quad \alpha = 0, 1, \dots, q-1, \quad (2)$$

where ρ and \mathbf{u} are macro density and velocity, respectively, and the ω_α is the weight coefficients corresponding to the discrete velocity, ξ_α .

In this work, the D2Q9 discrete velocity model, that is, 9 discrete velocities in two-dimensional physical space, is adopted and defined as the following:

$$\xi_\alpha = \begin{cases} (0, 0) & \alpha = 0, \\ (\cos[(\alpha-1)\pi/2], \sin[(\alpha-1)\pi/2])c & \alpha = 1, \dots, 4, \\ (\cos[(2\alpha-9)\pi/4], \sin[(2\alpha-9)\pi/4])\sqrt{2}c & \alpha = 5, \dots, 8, \end{cases} \quad (3)$$

where $c = \sqrt{3C_s^2} = 1$ is the lattice velocity.

A. AMR lattice Boltzmann scheme in the LBM domain

The LBE in Eq. (1) can be rewritten as^{36,37}

$$\frac{d}{ds} f_\alpha(\mathbf{x} + \xi_\alpha s, t + s) = -\frac{1}{\tau} (f_\alpha(\mathbf{x} + \xi_\alpha s, t + s) - f_\alpha^{eq}(\mathbf{x} + \xi_\alpha s, t + s)), \quad (4)$$

where the left side of Eq. (4) is a derivative along the characteristic $(\mathbf{x} + \xi_\alpha s, t + s)$. Integrating the Eq. (4) along the characteristic line $\mathbf{x}(s) = \mathbf{x} + \xi_\alpha s$ for a time interval from $s = 0$ to $s = \Delta t_l$ yields

$$\begin{aligned} & f_\alpha(\mathbf{x} + \xi_\alpha \Delta t_l, t + \Delta t_l) - f_\alpha(\mathbf{x}, t) \\ &= -\frac{1}{\tau} \int_0^{\Delta t_l} [f_\alpha(\mathbf{x} + \xi_\alpha s, t + s) - f_\alpha^{eq}(\mathbf{x} + \xi_\alpha s, t + s)] ds. \end{aligned} \quad (5)$$

Approximating the right-side integral form in Eq. (5) by the trapezium rule gives

$$\begin{aligned} & f_\alpha(\mathbf{x} + \xi_\alpha \Delta t_l, t + \Delta t_l) - f_\alpha(\mathbf{x}, t) \\ &= -\frac{\Delta t_l}{2\tau} [f_\alpha(\mathbf{x} + \xi_\alpha \Delta t_l, t + \Delta t_l) - f_\alpha^{eq}(\mathbf{x} + \xi_\alpha \Delta t_l, t + \Delta t_l) \\ &\quad + f_\alpha(\mathbf{x}, t) - f_\alpha^{eq}(\mathbf{x}, t)]. \end{aligned} \quad (6)$$

To change the implicit collision in Eq. (6) into explicit, an auxiliary distribution function $g_\alpha(\mathbf{x}, t)$ is introduced as the following:

$$g_\alpha(\mathbf{x}, t) = f_\alpha(\mathbf{x}, t) + \frac{\Delta t_l}{2\tau} (f_\alpha(\mathbf{x}, t) - f_\alpha^{eq}(\mathbf{x}, t)), \quad (7)$$

which is the so-called LBM distribution function and used in the present AMR lattice Boltzmann scheme. With the LBM distribution function $g_\alpha(\mathbf{x}, t)$, Eq. (6) can be rewritten as

$$g_\alpha(\mathbf{x} + \xi_\alpha \Delta t_l, t + \Delta t_l) - g_\alpha(\mathbf{x}, t) = -\frac{\Delta t_l}{\tau_l} (g_\alpha(\mathbf{x}, t) - g_\alpha^{eq}(\mathbf{x}, t)), \quad (8)$$

where the relaxation time τ_l in LBM is determined by $\tau_l = \tau + \Delta t_l/2$ and the equilibrium distribution function $g_\alpha^{eq}(\mathbf{x}, t) = f_\alpha^{eq}(\mathbf{x}, t)$. Then, the viscosity in the lattice Bhatnagar–Gross–Krook (LBGK) model is related to the relaxation time τ_l by

$$v_l = C_s^2 \left(\tau_l - \frac{\Delta t_l}{2} \right). \quad (9)$$

As the standard LBM, Eq. (8) is solved by two separate steps, that is, the collision and the stream procedures, in the present AMR lattice Boltzmann scheme. In the collision step, it gives

$$\hat{g}_\alpha(\mathbf{x}, t) = g_\alpha(\mathbf{x}, t) - \frac{\Delta t_l}{\tau_l} (g_\alpha(\mathbf{x}, t) - g_\alpha^{eq}(\mathbf{x}, t)), \quad (10)$$

where \hat{g}_α denotes the post-collision distribution functions. However, in the stream step, the Lax–Wendroff scheme^{5,38} is employed on non-uniform grids to achieve second-order accuracy of the AMRLBM and it can be given as

$$\begin{aligned} g_\alpha(\mathbf{x}, t + \Delta t_l) &= \frac{\sigma_l(1 + \sigma_l)}{2} \hat{g}_\alpha(\mathbf{x} - \xi_\alpha \Delta t_l, t) + (1 - \sigma_l^2) \hat{g}_\alpha(\mathbf{x}, t) \\ &\quad - \frac{\sigma_l(1 - \sigma_l)}{2} \hat{g}_\alpha(\mathbf{x} + \xi_\alpha \Delta t_l, t), \end{aligned} \quad (11)$$

where $\sigma_l = \frac{|\xi_\alpha| \Delta t_l}{\Delta x}$ is the CFL number of the AMRLBM, and $\Delta x, \Delta t_l$ are the grid spacing and the time step, respectively. It should be pointed out that the stream step in Eq. (11) becomes the same as it in the LBM when $\sigma_l = 1$, that is, $\Delta x = \Delta t_l$, which can only be satisfied when the spatial resolution is at its finest in the AMR lattice Boltzmann scheme.

Additionally, as the LBM, the macro velocity and density in the present AMR lattice Boltzmann scheme can be determined by

$$\tau_f = \tau_l - \frac{\Delta t_l}{2}, \quad (23)$$

where Δt_l is the time step of the LBM.

Furthermore, from Eq. (7), one can find that the distribution functions in the LBM domain and the FVLBM domain can be mutually transformed by the following way:

$$\begin{cases} g_x = f_x + \frac{\Delta t_l}{2\tau_f} (f_x - f_x^{eq}), \\ f_x = g_x - \frac{\Delta t_l}{2\tau_l} (g_x - g_x^{eq}), \end{cases} \quad (24)$$

where g_x and f_x are the distribution functions of LBM and FVLBM, respectively.

Equation (24) also defined the distribution function information exchange relations in the present coupling procedure of LBM and FVLBM domains. In addition to avoid the interpolation, both of the LBM domain and the FVLBM domain have one layer overlapped ghost cell around the interface, shown in Fig. 2, to store the exchanged distribution functions g_x, f_x in the present coupling procedure.

III. ADAPTIVE MESH REFINEMENT FOR LATTICE BOLTZMANN METHOD

In this section, a block-based adaptive mesh refinement strategy⁵ used in this work in the LBM domains is briefly introduced.

In the present AMR method, the root block to be refined is defined as a $L_x \times L_y$ domain with $n_x \times n_y$ square cells in the x and y

directions, respectively, and the refinement level at the root block is denoted as $l=0$. When a block is flagged for refinement, it will be isotropically sub-divided into four child blocks with a quad-tree structure upon each refinement, shown in Fig. 3. The grid types including flow, solid, and physical boundaries are defined by the relationship between the block and the geometry during the refinement. Furthermore, the refinement procedure is stopped until the prescribed finest refinement level l_{max} is achieved. In the refine meshes, all blocks consist of $n_x \times n_y$ cells, and the grid spacing of the cells is determined by the refinement level and the size of the root block, that is,

$$\Delta x = \frac{L_x}{n_x \times 2^l} = \frac{L_y}{n_y \times 2^l}, \quad (25)$$

where $n_x = n_y = 4$ is always used unless stated otherwise. Noteworthy, the maximum refinement level difference between the adjacent blocks needs to be equal to or less than 1; that is, the maximum refinement ratio is limited to $\Delta x_c/\Delta x_f = 2$, where the subscript c and f are the coarse and fine grid, respectively.

A. Data acquisition between adjacent blocks in AMRLBM

With the same idea in Ref. 39, the way to get data from adjacent blocks is by filling the auxiliary grids in the adjacent blocks. As depicted in Fig. 4, there are three situations for filling the auxiliary grids in the neighbor blocks.

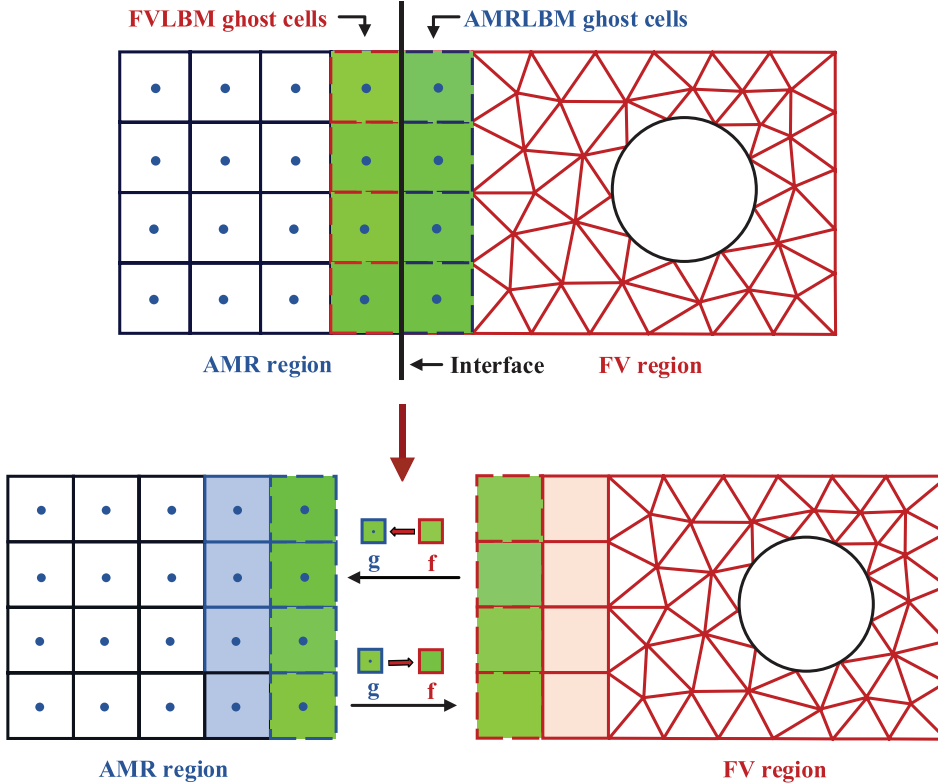
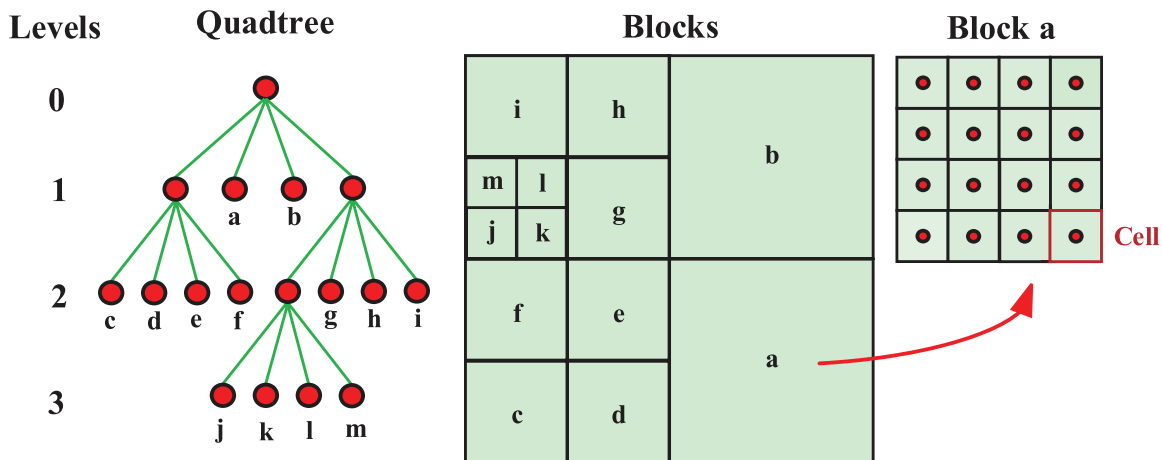


FIG. 2. Grid system of the hybrid scheme with two regions: AMR region (blue) and FV region (red).



Note: the refinement level difference for the adjacent blocks is limited to 1.

FIG. 3. Quad-tree structure in the present AMR lattice Boltzmann scheme.

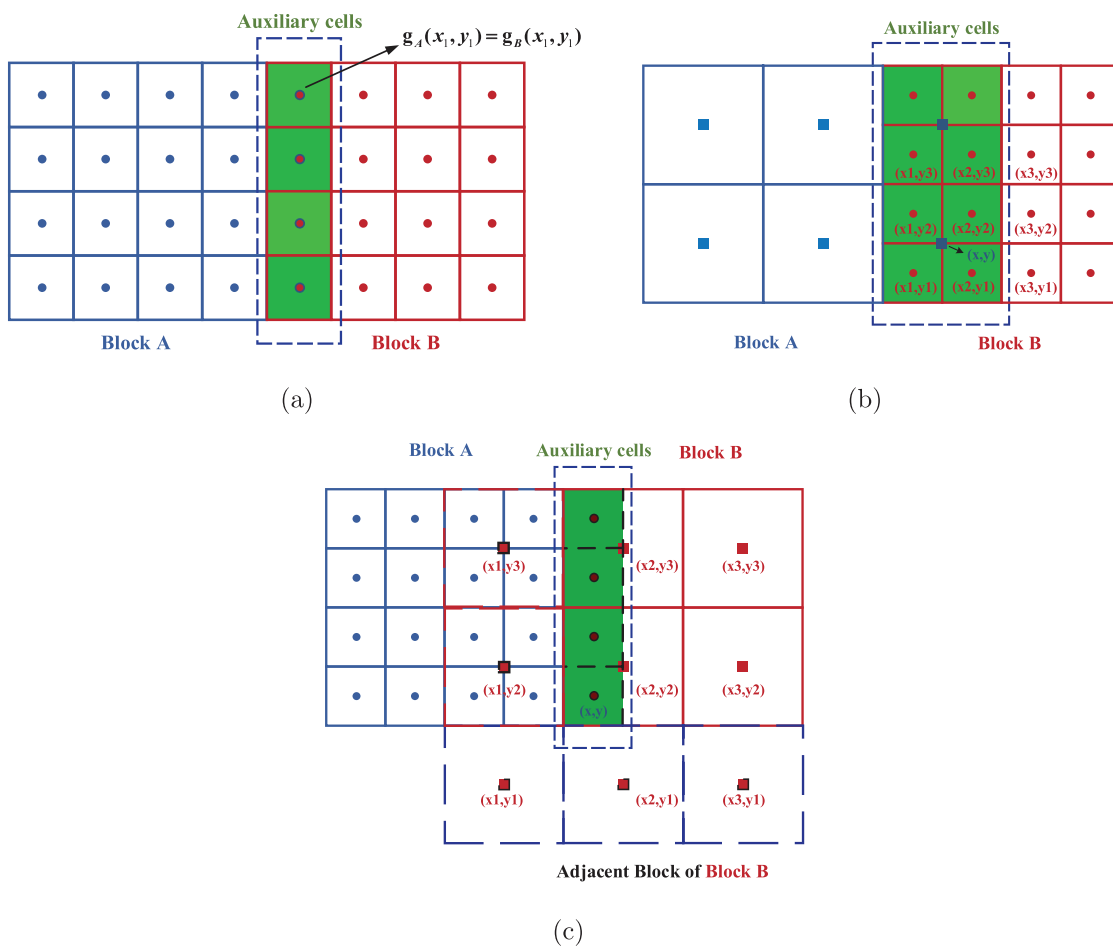


FIG. 4. Three situations for obtaining the distribution functions in auxiliary cells of block A from its adjacent block B: (a) case 1: $l_A = l_B$, (b) case 2: $l_B - l_A = 1$, and (c) case 3: $l_A - l_B = 1$.

The first case, as shown in Fig. 4(a), is that the two adjacent blocks have the same refinement level, that is, $l_A = l_B$. In this situation, the auxiliary cells of block A are completely overlapped with the associated neighbor cells in block B, and therefore, the distribution function $g_A(x_1, y_1)$ in auxiliary cells of block A can be directly assigned by the corresponding distribution function in block B located at (x_1, y_1) , that is,

$$g_A(x_1, y_1) = g_B(x_1, y_1). \quad (26)$$

The second case is displayed in Fig. 4(b), which shows that the resolutions of block A and its neighborhood block, that is, block B, are different and $l_B - l_A = 1$. In this condition, the distribution function $g_A(x, y)$ in auxiliary cells of block A is reconstructed by a biquadratic interpolation with the available distribution functions around the point (x, y) in block B, that is,

$$g_A(x, y) = \frac{1}{64} \begin{bmatrix} 3 & 6 & -1 \end{bmatrix} \begin{bmatrix} g_B(x_1, y_1) & g_B(x_1, y_2) & g_B(x_1, y_3) \\ g_B(x_2, y_1) & g_B(x_2, y_2) & g_B(x_2, y_3) \\ g_B(x_3, y_1) & g_B(x_3, y_2) & g_B(x_3, y_3) \end{bmatrix} \times \begin{bmatrix} 3 \\ 6 \\ -1 \end{bmatrix} + \mathcal{O}(\Delta x^3), \quad (27)$$

where (x_1, y_1) , (x_1, y_2) , (x_1, y_3) , (x_2, y_1) , (x_2, y_2) , (x_2, y_3) , (x_3, y_1) , (x_3, y_2) , and (x_3, y_3) are the interpolation stencil points in block B.

The third case is $l_A - l_B = 1$; that is, the resolution of block A is one level finer than the resolution of its neighboring block B. The auxiliary cells of block A is shown in Fig. 4(c). To obtain the distribution function $g_A(x, y)$ in the auxiliary cell of block A, the biquadratic interpolation is also adopted and

$$g_A(x, y) = \frac{1}{1024} \begin{bmatrix} 5 & 30 & -3 \end{bmatrix} \times \begin{bmatrix} g_B(x_1, y_1) & g_B(x_1, y_2) & g_B(x_1, y_3) \\ g_B(x_2, y_1) & g_B(x_2, y_2) & g_B(x_2, y_3) \\ g_B(x_3, y_1) & g_B(x_3, y_2) & g_B(x_3, y_3) \end{bmatrix} \begin{bmatrix} 5 \\ 30 \\ -3 \end{bmatrix} + \mathcal{O}(\Delta x^3), \quad (28)$$

where (x_1, y_1) , (x_2, y_1) , (x_3, y_1) , (x_1, y_2) , (x_1, y_3) , (x_2, y_2) , (x_2, y_3) , (x_3, y_2) , and (x_3, y_3) are the interpolation stencil points shown in Fig. 4(c).

B. Grid refinement/coarsening criteria in AMRLBM

In the present AMRLBM, dynamic refinement and coarsening techniques are used, and the dynamic refinement/coarsening procedure is triggered on a block by the value of an indicator ϵ , which is evaluated in a constant time intervals. In this work, we choose the module of the vorticity vector as the grid refinement/coarsening indicator

$$\epsilon_v = |\nabla \times \mathbf{v}| = \left| \frac{\delta v}{\delta x} - \frac{\delta u}{\delta y} \right|. \quad (29)$$

If the local ϵ for a block is above an upper threshold value $\sqrt{\langle \epsilon_v^2 \rangle}$, that is,

$$\epsilon_v > \sqrt{\langle \epsilon_v^2 \rangle}, \quad (30)$$

the block is flagged for grid refinement; by contrast, the block is marked for grid coarsening, while the local ϵ is below a lower threshold $0.1\sqrt{\langle \epsilon_v^2 \rangle}$, that is,

$$\epsilon_v < 0.1\sqrt{\langle \epsilon_v^2 \rangle}, \quad (31)$$

where $\sqrt{\langle \epsilon_v^2 \rangle}$ denotes the root mean square (RMS) value over the whole flow domain.

IV. COMPUTATIONAL RESULTS

In this section, three 2D steady incompressible flow cases, including (a) the Kovasznay flow, (b) the lid-driven cavity flow with $Re = 100, 400$, and 1000 , and (c) the steady flow past a cylinder with $Re = 20$ and 40 , are provided to validate the accuracy, stability, and efficiency of the proposed scheme. For all these simulations, the CFL number in the FV domain is set as $\sigma_f = 0.50$ unless stated otherwise and the convergence criteria for a steady state are defined as

$$E(\mathbf{u}) = \frac{\|\mathbf{u}(t) - \mathbf{u}(t - 1000\Delta t)\|_2}{\|\mathbf{u}(t)\|_2} < 10^{-12}, \quad \text{mod}(t, 1000\Delta t) = 0. \quad (32)$$

A. The Kovasznay flow

As the first numerical case, the steady Kovasznay flow⁴⁰ has analytical solutions and is often selected as a standard benchmark problem. In this work, it is used to evaluate the accuracy and convergence order of the present hybrid scheme. The analytical solutions of the Kovasznay flow for the macro velocity u^* , v^* , and macro pressure p^* are given as the following:

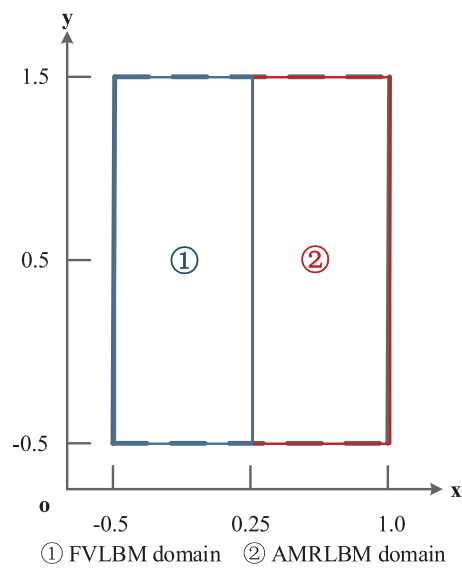


FIG. 5. Illustration of the flow domain of the Kovasznay flow.

$$\begin{aligned} u^* &= U_0 [1 - e^{i\lambda x} \cos(2\pi y)], \\ v^* &= \frac{\lambda U_0}{2\pi} e^{i\lambda x} \sin(2\pi y), \\ p^* &= \frac{U_0^2}{2} (1 - e^{2i\lambda x}), \end{aligned} \quad (33)$$

where $\lambda = \frac{U_0}{2\nu} - \sqrt{\frac{U_0^2}{4\nu^2} + 4\pi^2}$, and U_0 is the maximal velocity.

In this case, the Reynolds number is set as $Re = U_0 L / \nu = 40$, and the maximal velocity and the reference length are fixed at $U_0 = 0.01$ and $L = 2.0$, respectively. As illustrated in Fig. 5, the flow domain is designed as a rectangle box with $(x, y) \in [-0.5, 1.0] \times [-0.5, 1.5]$, where the left half region $(x, y) \in [-0.5, 0.25] \times [-0.5, 1.5]$ is covered with the FV domain and the right half region $(x, y) \in [0.25, 1.0] \times [-0.5, 1.5]$ is devised as the AMRLBM domain. Furthermore, two Dirichlet boundary conditions with the exact solutions are applied to $x = -0.5$ and 1.0 and two periodic boundary conditions are put at $y = -0.5$ and 1.5 .

To compute the convergence order of the present hybrid scheme, simulations are carried out for five sequentially refined meshes. To be

concrete, uniform meshes are adopted in the FVLBM domain and the associated grid sizes are $\Delta x = 1/32, 1/48, 1/64, 1/96$, and $1/128$, respectively, for the five sequentially refined meshes. For the grid sizes with $\Delta x = 1/48$ and $1/96$, a block consists of $n_x \times n_y = 6 \times 6$ cells in the AMRLBM meshes. In the AMRLBM domain, grid size of $2\Delta x$ is initially adopted. As shown in Fig. 6, to reduce the cost of data exchange between the FVLBM and AMRLBM, the meshes in the left $2/3$ part of the AMRLBM domain have been refined to the same grid sizes of the FVLBM domain.

Figure 7 shows the numerical results of velocities contours simulated with $\Delta x = 1/128$ in the FVLBM domain. In this figure, it also depicts the analytical solutions of velocities with dashed white lines. From Fig. 7, it can be clearly seen that the dashed white lines perfectly coincide with the black contour lines, which reveals that there is an excellent agreement between the numerical and the analytic results and the present hybrid scheme can provide accurate numerical results.

To obtain the convergence order of the present hybrid scheme, we compute the L_2 error of u , which is defined as

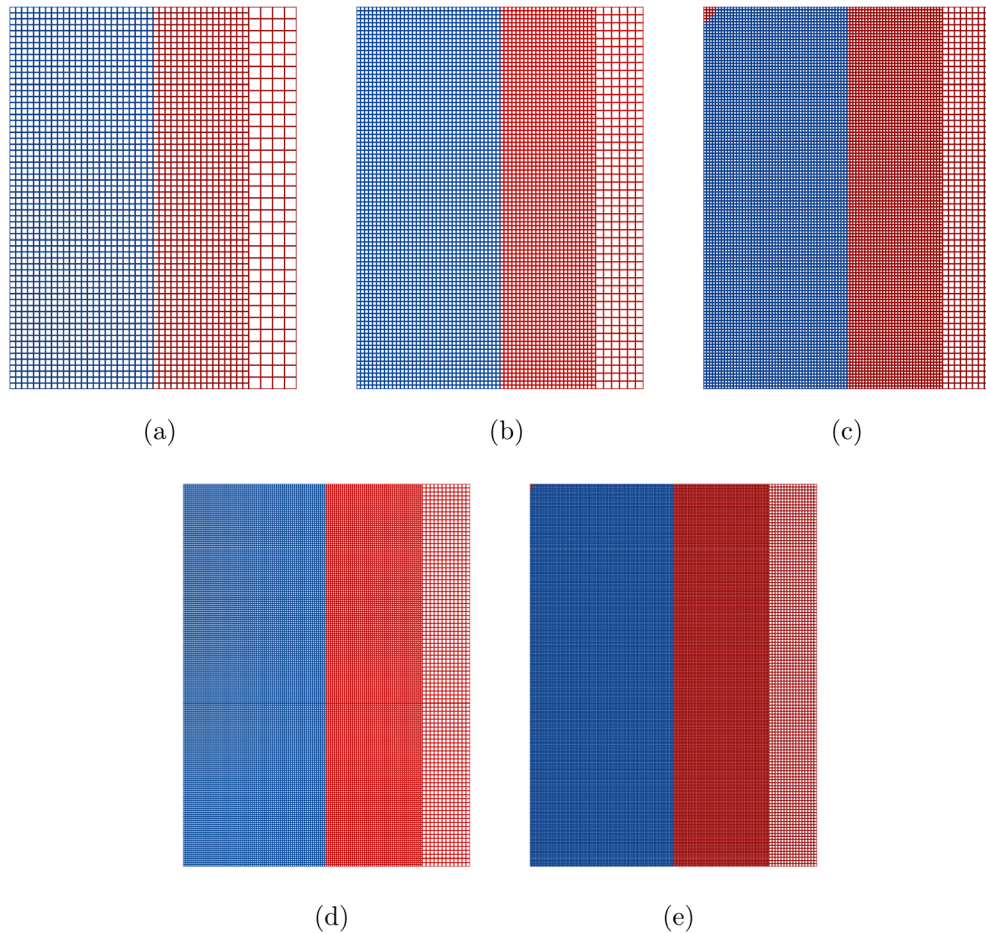


FIG. 6. Five kinds of meshes of the Kovasznay flow, including the AMR grids (red) and the FV grids (blue): (a) cell number 2688 with $\Delta x = 1/32$ in FVLBM domain, (b) cell number 6048 with $\Delta x = 1/48$ in the FVLBM domain, (c) cell number 10 752 with $\Delta x = 1/64$ in the FVLBM domain, (d) cell number 24 192 with $\Delta x = 1/96$ in the FVLBM domain, and (e) cell number 43 008 with $\Delta x = 1/128$ in the FVLBM domain.

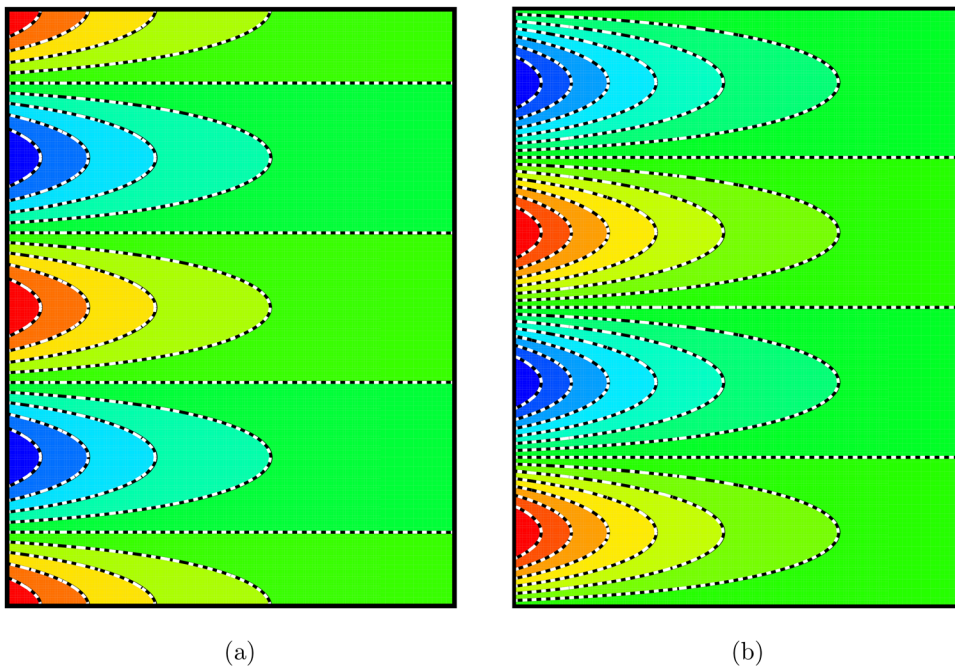


FIG. 7. Velocity contours of the steady Kovasznay flow at $\text{Re} = 40$, where the white dashed and the black solid lines denote analytical and numerical solutions of velocity contours, respectively: (a) the velocity contours for u -component and (b) the velocity contours for v -component.

$$\|\delta u\|_2 = \|u - u^*\|_2 = \sqrt{\frac{1}{N_{\text{cell}}} \sum_{i=1}^{N_{\text{cell}}} (u_i - u_i^*)^2}, \quad (34)$$

where N_{cell} denotes the number of grid cells in the whole flow field, and u and u^* are the numerical velocity and the analytical solutions computed in Eq. (33), respectively. From the numerical analysis, the L_2 error and the number of degrees of freedom (DOF) satisfy the following identity:

$$\|\delta u\|_2 = C(\sqrt{DOF})^{-K}, \quad (35)$$

where C is a constant number, K is the convergence order, and $d=2$ is dimensional space. The simulated result of $\log(L_2)$ vs $\log(\sqrt{DOF})$ is plotted in Fig. 8 by using Eq. (35) and the linear least squares fitting technique, and one can obtain the convergence order $K_u \approx 2.199$, which verifies that the present hybrid scheme has second-order accuracy.

B. The lid-driven square cavity flow

The second illustrating case we choose is the 2D lid-driven square cavity flow. In this case, there is a closed square cavity in which the

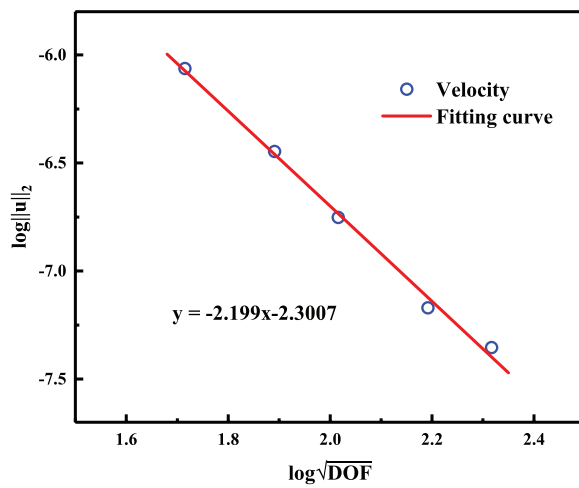


FIG. 8. L_2 -norm of error in u -velocity.

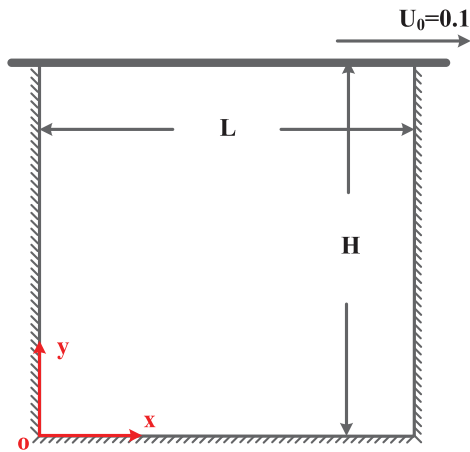


FIG. 9. Sketch of the flow domain for the lid-driven cavity flow.

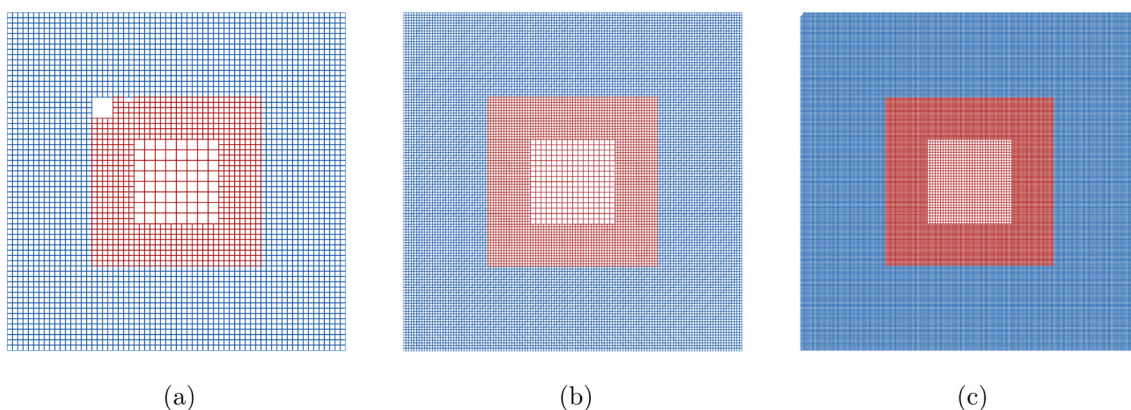


FIG. 10. Three kinds of meshes of the lid-driven cavity flow, including the AMR grids (red) and the FV grids (blue): (a) mesh-1 with $\Delta x = 1/64$ in FVLM domain, (b) mesh-2 with $\Delta x = 1/128$ in FVLM domain, and (c) mesh-3 with $\Delta x = 1/256$ in FVLM domain.

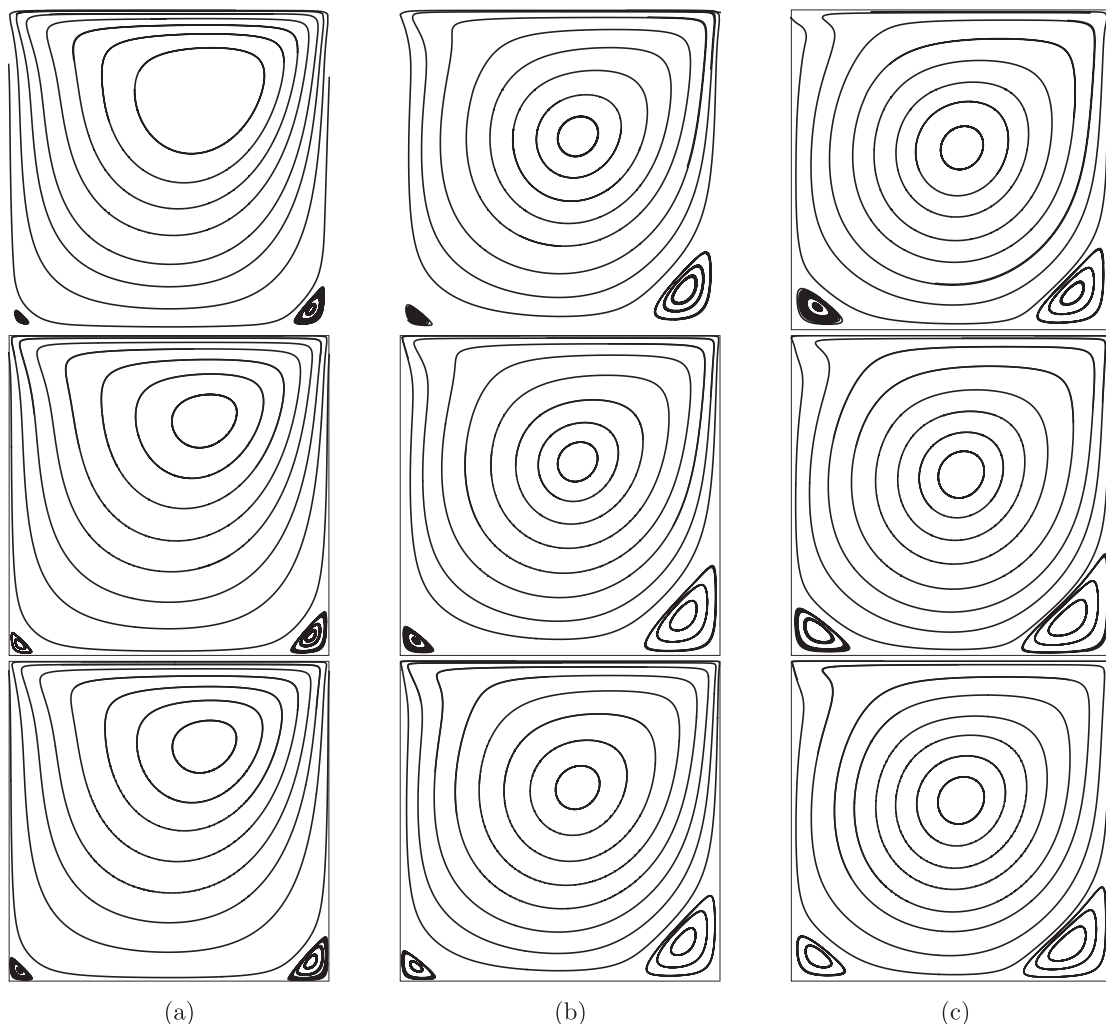


FIG. 11. The streamline of the lid-driven cavity flow. Flow left to right: streamlines at (a) $Re = 100$, (b) $Re = 400$, and (c) $Re = 1000$. From top to bottom: streamlines at mesh-1, mesh-2, and mesh-3.

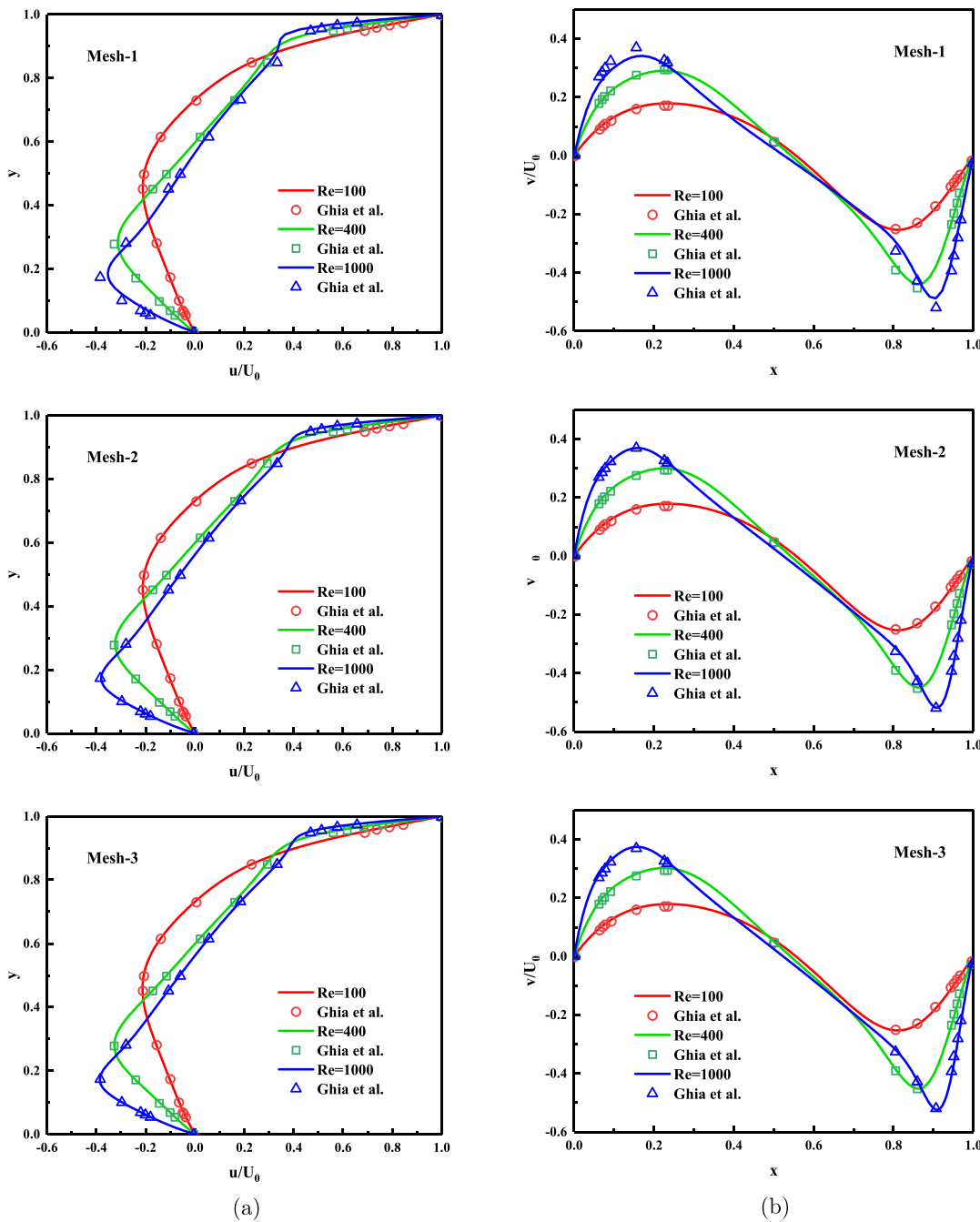


FIG. 12. Velocity profiles at $Re = 100, 400$, and 1000 through the cavity geometric center. Flow left to right: (a) the velocity component u/U_0 along $x = 0.5$, (b) the velocity component v/U_0 along $y = 0.5$. From top to bottom: velocity profiles obtained by the mesh-1, mesh-2, and mesh-3.

bottom and two side walls are static and the top wall is horizontally moving with a constant velocity U_0 . The geometric information is shown in Fig. 9. The computational domain is devised as a region $(x, y) \in [0.0, 1.0] \times [0.0, 1.0]$, that is, $L = H = 1.0$. As for the boundaries of the cavity, there is a driven horizontal velocity $U_0 = 0.1$ exerted at the top wall, that is, $y = 1.0$, and three no-slip boundaries are set at

the bottom, left, and right walls, that is, $y = 0.0$, $x = 0.0$, and $x = 1.0$, respectively. Moreover, simulations with $Re = U_0 L / v = 100, 400$, and 1000 are conducted.

In this case, three kinds of gradually refined meshes are adopted and the sketch of the meshes is given in Fig. 10. Among these meshes, the AMR region is fixed and located at $(x, y) \in [0.25, 0.75] \times [0.25, 0.75]$,

whereas the rest FV domain is filled by uniform grids. Specifically, for these three meshes, in the AMRLBM domain, the minimum refinement level is set as $l_{min} = 3$, $l_{min} = 4$, and $l_{min} = 5$, which corresponded to the grid sizes of 1/32, 1/64, and 1/128 for mesh-1, mesh-2, and mesh-3, respectively. Additionally, the maximum refinement levels in the AMRLBM domains are chosen as $l_{max} = 4$, $l_{max} = 5$, and $l_{max} = 6$ and the associated grid sizes are 1/64, 1/128, and 1/256, respectively. Furthermore, the grid sizes of the corresponding FV domains in these three kinds of meshes are $\Delta x = 1/64, 1/128$, and 1/256, respectively.

The simulated streamlines at Reynolds numbers $Re = 100, 400$, and 1000 with mesh-1, mesh-2, and mesh-3 are sketched in Fig. 11. In the figure, it shows that there are three vortices in the cavity, including a primary and two secondary vortices located in the center and two bottom corner of the cavity in all cases. In addition, the figure also shows that the center of the primary vortex gradually approaches to the centroid of the cavity and two secondary vortices become stronger as the Reynolds number Re increases. Therefore, it can be easily seen that the observations in this figure agree with the benchmark results⁴¹ very well.

For further quantitative comparison of numerical results, the profile of non-dimensional velocity components u/U_0 and v/U_0 along the vertical and horizontal center lines at various Reynolds numbers for mesh-1, mesh-2, and mesh-3 are plotted in Fig. 12. As shown in Fig. 12, the difference between the numerical and the benchmark results decreases as the grid resolution increases, and the numerical results for mesh-2 and mesh-3 are almost identical, which gives grid convergent results. Additionally, the position of the primary and two secondary vortices calculated by the present hybrid scheme and the benchmark data^{41–43} are listed in Table I. From the table, one can find that the locations of the vortices calculated by the present scheme have excellent agreement with previous available results, which shows that

the present hybrid scheme is an accurate and reliable tool for incompressible flows.

To check the ability of the present hybrid scheme to suppress unphysical pressure oscillations, a comparison study between the present hybrid scheme and the standard LBM is made. We simulated the present lid-driven cavity flow at $Re = 1000$ with mesh-3 by the present hybrid scheme and a 256×256 uniform grid by LBM. The simulated pressure contours are shown in Figs. 13(a) and 13(c). In addition, the enlarged pressure contours in the domain near the upper-left corner, that is, $(x, y) \in [0.0, 0.15] \times [0.85, 1.0]$, are sketched in Figs. 13(b) and 13(d) for the LBM result and the result of the present hybrid scheme, respectively. These figures clearly show that some pressure oscillations occur near the upper-left corner in the LBM result, while smooth pressure contours are given in such a region in the result of the present hybrid scheme. The reason for this difference comes from two aspects. One is that the present LBM uses the lattice BGK model, which is not so stable for relatively high Re flows.⁴⁴ Another is that the FVLBM generally has much larger numerical dissipations than the associated LBM, which can suppress the unphysical pressure oscillations.¹⁷

These figures clearly show that some pressure oscillations occur near the upper-left corner in the LBM result, while smooth pressure contours are given in such a region in the result of the present hybrid scheme. Hence, it can be concluded that, compared with the LBM, the present hybrid scheme has better numerical stability.

C. Steady laminar flow past a circular cylinder

To investigate the ability of the present hybrid scheme to simulate flows with complex geometry, the case of steady laminar flow over a circular cylinder is adopted in this work. The geometry and the

TABLE I. The center location (x, y) of the primary and two secondary vortices with different grid resolutions.

| Re | | Primary vortex (x, y) | Lower-left secondary vortex (x, y) | Lower-right secondary vortex (x, y) |
|-----------|----------------------------------|------------------------------|---|--|
| Re = 100 | Ghia <i>et al.</i> ⁴¹ | (0.6172, 0.7344) | (0.0313, 0.0391) | (0.9453, 0.0625) |
| | Vanka ⁴² | (0.6188, 0.7375) | (0.0375, 0.0313) | (0.9375, 0.0563) |
| | Hou <i>et al.</i> ⁴³ | (0.6196, 0.7373) | (0.0392, 0.0353) | (0.9451, 0.0627) |
| | Mesh-1 | (0.6157, 0.7379) | (0.0369, 0.0372) | (0.9422, 0.0643) |
| | Mesh-2 | (0.6153, 0.7372) | (0.0352, 0.0355) | (0.9424, 0.0621) |
| | Mesh-3 | (0.6155, 0.7373) | (0.0344, 0.0349) | (0.9425, 0.0616) |
| Re = 400 | Ghia <i>et al.</i> ⁴¹ | (0.5547, 0.6055) | (0.0508, 0.0469) | (0.8906, 0.1250) |
| | Vanka ⁴² | (0.5563, 0.6000) | (0.0500, 0.0500) | (0.8875, 0.1188) |
| | Hou <i>et al.</i> ⁴³ | (0.5608, 0.6078) | (0.0549, 0.0510) | (0.8902, 0.1255) |
| | Mesh-1 | (0.5548, 0.6038) | (0.0521, 0.0456) | (0.8879, 0.1239) |
| | Mesh-2 | (0.5541, 0.6052) | (0.0514, 0.0469) | (0.8856, 0.1231) |
| | Mesh-3 | (0.5539, 0.6054) | (0.0510, 0.0471) | (0.8853, 0.1227) |
| Re = 1000 | Ghia <i>et al.</i> ⁴¹ | (0.5313, 0.5625) | (0.0859, 0.0781) | (0.8594, 0.1094) |
| | Vanka ⁴² | (0.5438, 0.5625) | (0.0750, 0.0813) | (0.8625, 0.1063) |
| | Hou <i>et al.</i> ⁴³ | (0.5333, 0.5647) | (0.0902, 0.0784) | (0.8667, 0.1137) |
| | Mesh-1 | (0.5337, 0.5692) | (0.0826, 0.0718) | (0.8785, 0.1129) |
| | Mesh-2 | (0.5313, 0.5657) | (0.0835, 0.0773) | (0.8653, 0.1123) |
| | Mesh-3 | (0.5307, 0.5653) | (0.0833, 0.0778) | (0.8638, 0.1121) |

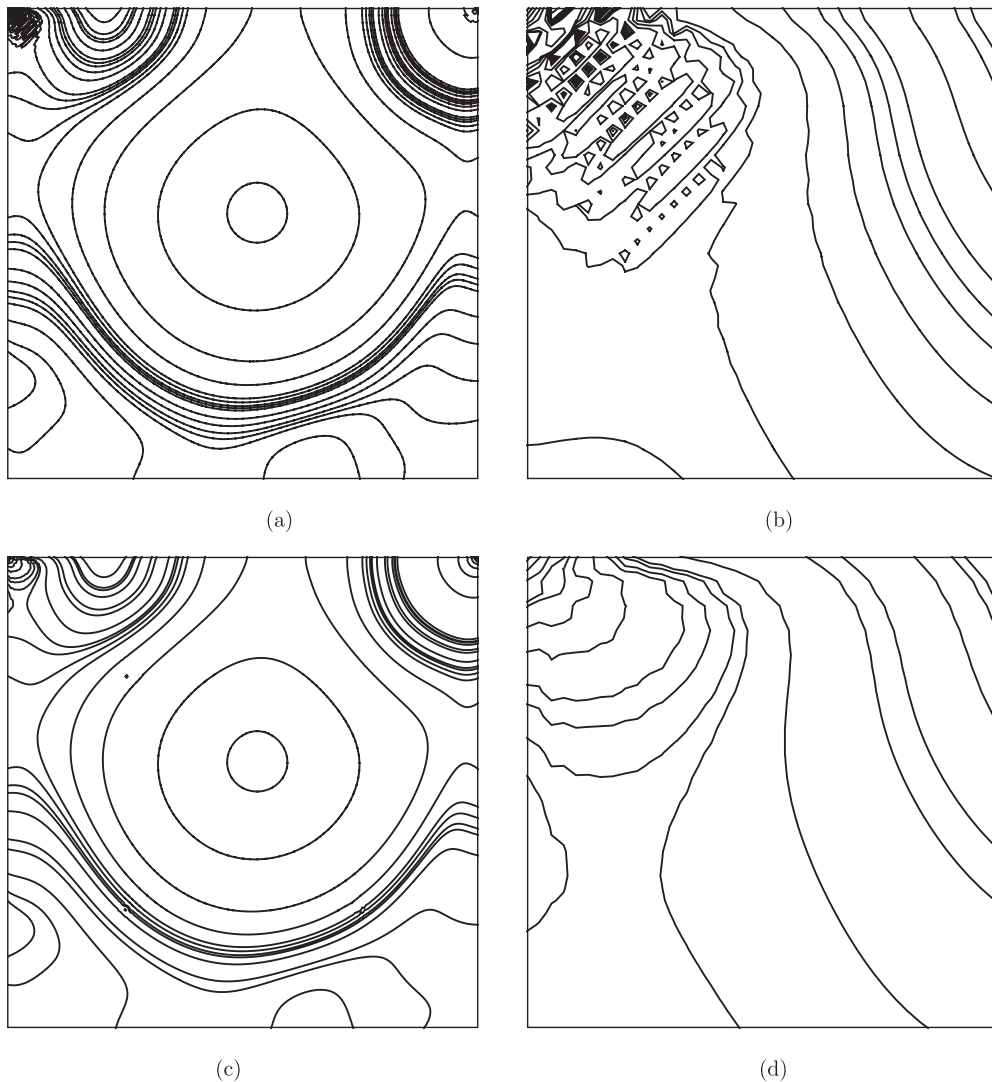


FIG. 13. The contours of the pressure p at $\text{Re} = 1000$: (a) the standard LBM result with $N^2 = 256 \times 256$; (c) the present hybrid scheme result with mesh-3; (b) and (d) the enlarged view of the p contours in the upper-left corner ($x, y \in [0.0, 0.15] \times [0.85, 1.0]$) in (a) and (c), respectively.

devised computational domain are illustrated in Fig. 14, where the diameter of the cylinder is $D = 2R$ and the computational domain is $L \times H = 60D \times 40D$. Additionally, the centroid of the cylinder is located at a position, which is $20D$ far from the left inlet boundary. In the simulation, the Reynolds numbers $\text{Re} = U_\infty D / \nu$ are set as $\text{Re} = 20$ and 40 , where $U_\infty = 0.1$ and $D = 1.0$.

In this case, as shown in Fig. 14, the computational domain is divided into two parts: the FVLBM part and the AMRLBM part. The FVLBM part is surrounding the cylinder and covers the region $L_1 \times H_1 = 2D \times 2D$, while the AMRLBM part covers the rest part of the computational domain. Moreover, on the top and bottom and left boundaries of the computational domain, there are inlet boundary conditions with a specified velocity $\mathbf{U} = (U_\infty, 0)$. On the right boundary of the domain, an outlet boundary condition with a specified pressure $\rho_\infty = 1.0$ is set. In addition to these outer boundaries, there is an

inner boundary, that is, the cylinder wall, on which no-slip boundary conditions are imposed.

The computational mesh is shown in Fig. 15. Specifically, in the FV region, the mixed meshes including quadrilateral boundary layer meshes, unstructured triangular meshes outside of the boundary layer, and some square cells adjacent with the AMR domain. For the boundary layer cells, the grid sizes along normal directions of the cylinder wall are specified by a geometric sequence for which the mesh sizes are determined by the first grid layer height h_0 and the growth ratio r . In this case, three kinds of h_0 and r are used to generate the meshes and they are listed in Table II. As for the AMR region, the grid with the refinement levels ranging from $l_{\min} = 6$, $\Delta x = 0.25$ to $l_{\max} = 9$, $\Delta x = 0.03125$ is adopted.

In the simulation, normalized separation length L_s/R , separation angle θ_s , and drag coefficient C_d are calculated for comparison with

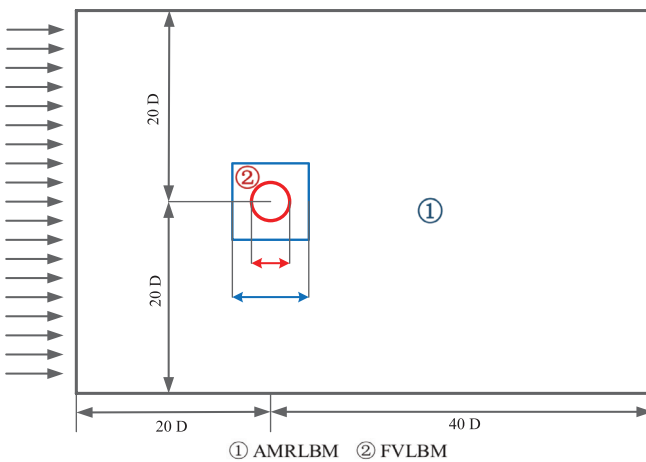


FIG. 14. Schematic of the computational domain for the flow past a 2D circular cylinder.

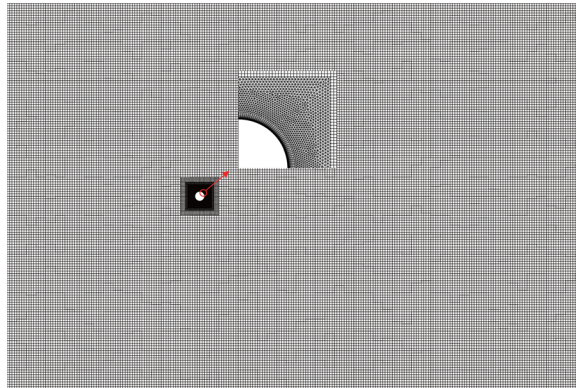
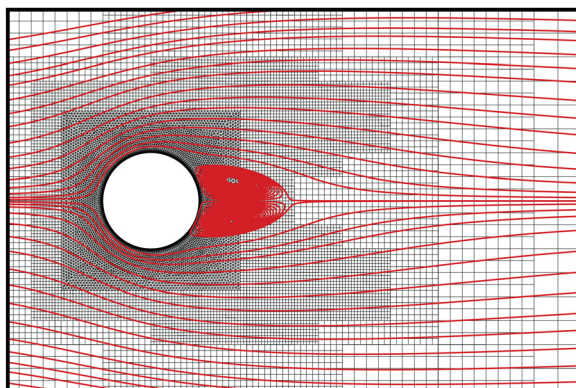
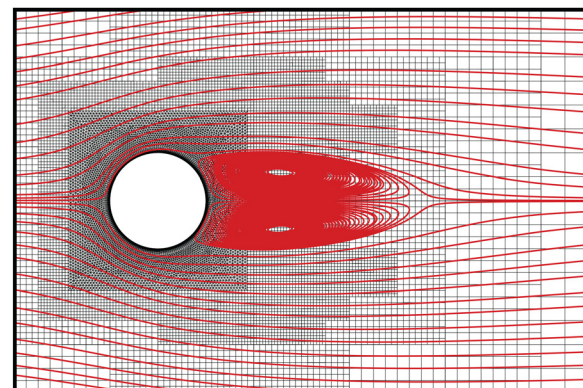


FIG. 15. Hybrid unstructured mesh for the flow past a 2D cylinder with mesh-1.



(a)



(b)

FIG. 16. Streamlines of the 2D cylinder flow at (a) $\text{Re} = 20$ and (b) $\text{Re} = 40$.

TABLE II. Parameters, that is, h_0/D and r , for the boundary layer meshes.

| Mesh | h_0/D | r |
|--------|----------------------|------|
| Mesh-1 | 1.0×10^{-3} | 1.20 |
| Mesh-2 | 2.0×10^{-3} | 1.20 |
| Mesh-3 | 2.0×10^{-3} | 1.15 |

previous experiment and numerical results.^{14,45–48} The drag coefficient C_d defined as

$$C_d = \frac{F_x}{\frac{1}{2} \rho_\infty U_\infty^2 D}, \quad (36)$$

where the drag force F_x is the streamwise component of the hydrodynamic force of F , and

$$F = \oint_{\partial\Omega} (-p\mathbf{I} + 2\rho v \mathbf{S}) \cdot \hat{\mathbf{n}} \, dA, \quad (37)$$

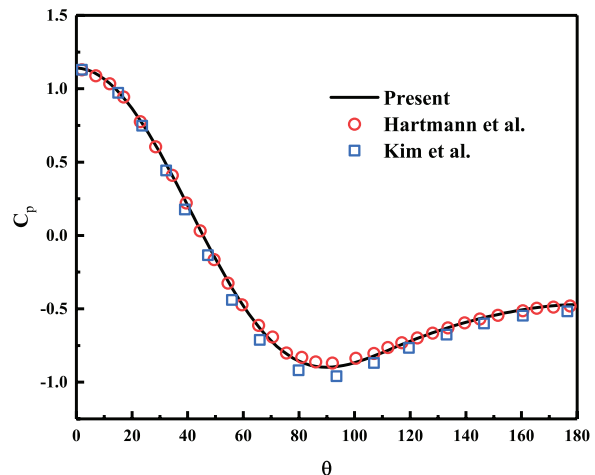
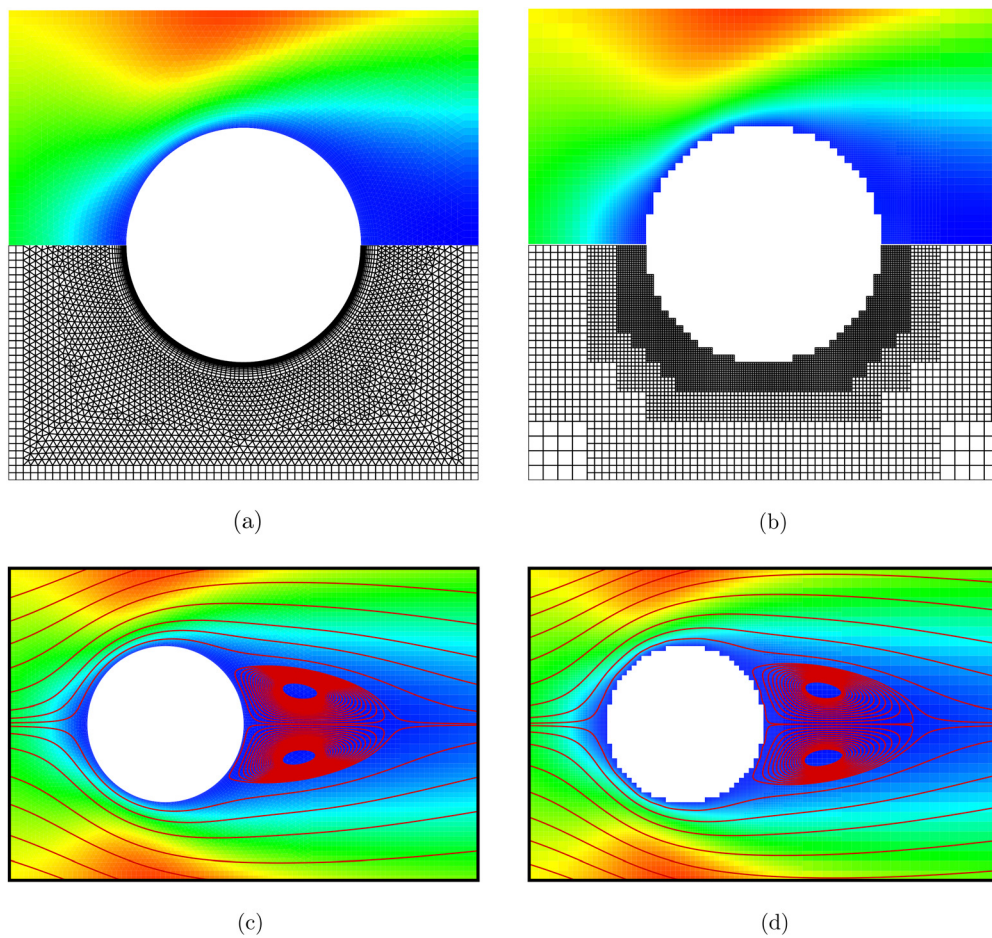
where $p = \rho/C_s^2$, $\mathbf{S}_{\alpha\beta} = \frac{1}{2}(\partial_\alpha u_\beta + \partial_\beta u_\alpha)$, and $\hat{\mathbf{n}}$ are the pressure, the stress tensor, and the out-normal unit vector of the cylinder boundary $\partial\Omega$, respectively.

Simulated streamlines at $\text{Re} = 20$ and 40 with the mesh-2 are depicted in Fig. 16. It can be clearly seen that there is a pair of stationary vortices behind the cylinder at both $\text{Re} = 20$ and $\text{Re} = 40$ and the separation length and the separation angle of the recirculation zone increase as the Reynolds number Re grows, which has qualitatively agreement with available results.^{14,47,48} Simulated normalized separation length L_s/R , separation angle θ_s , and drag coefficient C_d at $\text{Re} = 20$ and 40 are given in Table III. Moreover, the simulated pressure coefficient $C_p(\theta) = [p(\theta) - p_\infty]/frac{1}{2}\rho_\infty U_\infty^2$ on the cylinder wall at $\text{Re} = 40$ with the mesh-2 and the reference data^{49,50} are plotted in Fig. 17. From the comparisons in Table III and Fig. 17, excellent agreements with previous experiment and numerical results can be observed, which implies that the present hybrid scheme can be accurate for flows with complex geometries.

TABLE III. Simulation results of the flow over a circular cylinder at $Re = 20$ and 40.

| | $Re = 20$ | | | $Re = 40$ | | |
|----------------------|-----------|------------|-------|-----------|------------|-------|
| | L_s/R | θ_s | C_d | L_s/R | θ_s | C_d |
| Exp. ⁴⁵ | ... | ... | 2.08 | ... | ... | 1.58 |
| Exp. ⁴⁶ | 1.86 | 44.8° | ... | 4.26 | 53.5° | ... |
| IS-LBE ⁴⁷ | 1.842 | 42.96° | 2.152 | 4.490 | 52.84° | 1.499 |
| FD-LBE ⁴⁸ | 1.8480 | 43.58° | 2.021 | 4.510 | 51.86° | 1.515 |
| FV-LBE ¹⁴ | 2.0376 | 44.70° | 2.118 | 4.7027 | 54.65° | 1.568 |
| Mesh-1 | 1.863 | 43.66° | 2.043 | 4.469 | 53.44° | 1.513 |
| Mesh-2 | 1.857 | 43.37° | 2.046 | 4.424 | 53.54° | 1.517 |
| Mesh-3 | 1.872 | 43.67° | 2.045 | 4.476 | 53.59° | 1.515 |
| AMRLBM | 1.942 | 43.81° | 2.060 | 4.655 | 53.17° | 1.548 |

To further evaluate the efficacy of the present hybrid method for dealing with flows with complex geometries, a comparison study between the present hybrid method with mesh-1 and the AMRLBM is made and simulations by present hybrid method and the AMRLBM

**FIG. 17.** Pressure coefficient distribution $C_p(\theta)$ at $Re = 40$. The compared data were published by Hartmann et al.⁴⁹ and Kim et al.⁵⁰**FIG. 18.** The u -component velocity contours and the streamlines computed by the hybrid mesh [left, i.e., (a) and (c)] and the AMR mesh [right, i.e., (b) and (d)] at $Re = 20$.

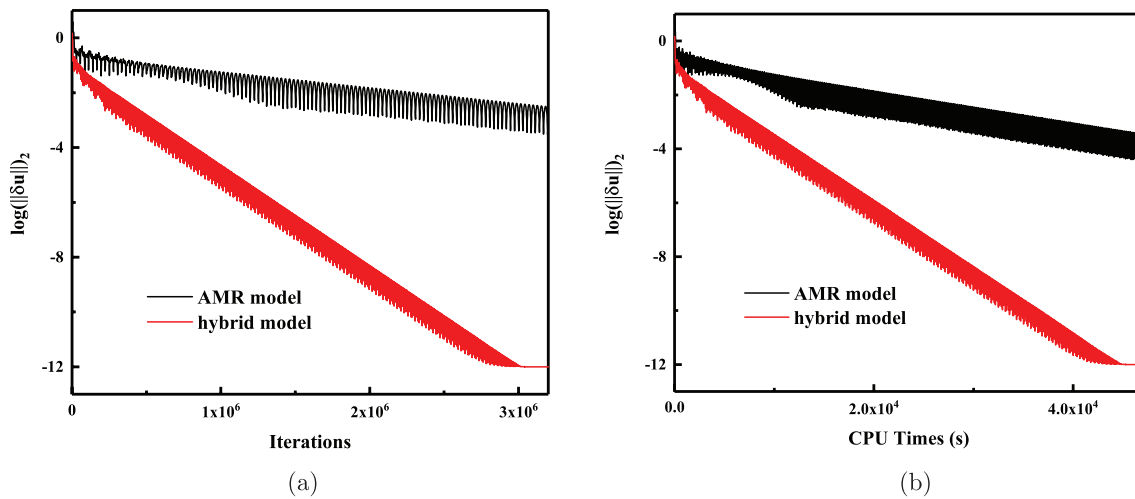


FIG. 19. Convergence histories of u-component velocity computed by the present hybrid scheme (red) and the AMRLBM (black) for the flow past a 2D cylinder at $Re = 20$: (a) $\log(||\delta u||_2)$ vs the number of iterations n and (b) $\log(||\delta u||_2)$ vs the CPU time T_{CPU} .

for the present 2D steady circular cylinder flow at $Re = 20$ and 40 are carried out. At $Re = 20$, the grid number of the mesh-1 and the AMRLBM mesh are 57 812 and 56 704, respectively. In the simulation, the computation domain is the same as the domain shown in Fig. 14 and, for the AMRLBM simulation, the whole domain is covered by the AMR grids and the refinement levels are ranging from $l_{min} = 6$ to $l_{max} = 11$. The simulation results by the proposed hybrid method and the AMRLBM in terms of the normalized separation length L_s/R , the separation angle θ_s , and the drag coefficient C_d are also listed in Table III. Table III shows that the AMRLBM results and the numerical results of the proposed hybrid method agree well with the available experiment and numerical results,^{14,45–48} but the agreement between the numerical results by the proposed hybrid method and the available experiment and numerical results can be better. The simulated u-component velocity contours near the cylinder at $Re = 20$ are plotted in Figs. 18(a) and 18(b) for the proposed hybrid method and the AMRLBM, respectively. The associated streamlines are sketched in Figs. 18(c) and 18(d). These figures clearly indicate that there is an important advantage for the present hybrid method over the AMRLBM that the curve boundary profile can be accurately represented by a smooth rather than stepped surface, which greatly improves the ability of the LBM to deal with the flows involving complex geometries. Additionally, the convergence histories of these two methods in terms of the u-component velocity, that is, $\log(||\delta u||_2)$ vs the number of iterations n and $\log(||\delta u||_2)$ vs the CPU time T_{CPU} , are recorded in Fig. 19, which reveals that the present hybrid method converges much faster than the AMRLBM. Therefore, it can be concluded that the present hybrid scheme can be more accurate and efficient than the AMRLBM for incompressible flows with complex geometries.

V. CONCLUSION

In this paper, a new hybrid lattice Boltzmann method, which couples the AMRLBM and FVLBM for steady incompressible flows with complex geometries, was presented. In the present scheme, the computational domain is generally divided into two non-overlapped

parts: the FVLBM domain and the AMRLBM domain. In the FVLBM domain, where the complicated boundary geometries are included, the efficient gas-kinetic BGK scheme base FVLBM is adopted to simulate the flow. In the AMRLBM domain, which generally covers the rest of the computational domain, the AMRLBM is utilized to find the flow solutions. The coupling between these two domains is through directly distribution function information exchange without complicated reconstruction, which was often adopted in conventional hybrid lattice Boltzmann schemes.

The proposed scheme has been validated by three steady cases in two dimensions including (a) the Kovasznay flow, (b) the lid-driven cavity flow, and (c) the laminar flow past a circular cylinder. Specifically, the steady Kovasznay flow is used to compute the convergence orders of the present hybrid scheme and the numerical results show that the convergence order is $K_u \approx 2.199$. The lid-driven cavity flow at $Re = 100$, 400, and 1000 is used to further demonstrate the accuracy and numerical stability. Moreover, the effectiveness for handling flows with complex geometries was further justified by simulation of the laminar flow past a circular cylinder at $Re = 20$ and 40 and making comparisons with the AMRLBM. The numerical results clearly show that the proposed hybrid method can give a remarkable performance in terms of the accuracy, the numerical stability, the computation efficiency, and the flexibility for dealing with the complex geometries. Therefore, the present hybrid scheme could be a reliable tool for the steady incompressible flows and could be applied to the engineering applications easily.

Finally, we noted that while the present hybrid scheme is mainly devised for steady flows, it can also be potentially extended to simulate incompressible unsteady flows, which will be one of our ongoing research topics.

ACKNOWLEDGMENTS

The authors are grateful to the financial support from the National Key Research and Development Program of China (No. 2017YFC0805703). The authors would like to thank the associated

editor and the anonymous reviewers for their valuable comments and suggestions to improve the quality of the paper.

AUTHOR DECLARATIONS

Conflict of Interest

The authors have no conflicts to disclose.

DATA AVAILABILITY

The data that support the findings of this study are available from the corresponding authors upon reasonable request.

REFERENCES

- ¹X. He and L.-S. Luo, "A priori derivation of the lattice Boltzmann equation," *Phys. Rev. E* **55**, R6333(R) (1997).
- ²X. He and L.-S. Luo, "Theory of the lattice Boltzmann method: From the Boltzmann equation to the lattice Boltzmann equation," *Phys. Rev. E* **56**, 6811–6817 (1997).
- ³H. Chen, O. Filippova, J. Hoch, K. Molvig, R. Shock, C. Teixeira, and R. Zhang, "Grid refinement in lattice Boltzmann methods based on volumetric formulation," *Physica A* **362**, 158–167 (2006).
- ⁴G. Eitel-Amor, M. Meinke, and W. Schröder, "A lattice-Boltzmann method with hierarchically refined meshes," *Comput. Fluids* **75**, 127–139 (2013).
- ⁵A. Fakhari and T. Lee, "Numerics of the lattice Boltzmann method on nonuniform grids: Standard LBM and finite-difference LBM," *Comput. Fluids* **107**, 205–213 (2015).
- ⁶X. Chen, Z. Chai, H. Wang, and B. Shi, "A finite-difference lattice Boltzmann method with second-order accuracy of time and space for incompressible flow," *Comput. Math. Appl.* **80**, 3066–3081 (2020).
- ⁷S. T. Kis and V. E. Ambruš, "Implicit-explicit finite-difference lattice Boltzmann model with varying adiabatic index," *AIP Conf. Proc.* **2218**, 050008 (2020).
- ⁸W. Li and L.-S. Luo, "An implicit block LU-SGS finite-volume lattice-Boltzmann scheme for steady flows on arbitrary unstructured meshes," *J. Comput. Phys.* **327**, 503–518 (2016).
- ⁹W. Li and W. Li, "A gas-kinetic BGK scheme for the finite volume lattice Boltzmann method for nearly incompressible flows," *Comput. Fluids* **162**, 126–138 (2018).
- ¹⁰W. Li, W. Li, P. Song, and H. Ji, "A conservation-moment-based implicit finite volume lattice Boltzmann method for steady nearly incompressible flows," *J. Comput. Phys.* **398**, 108882 (2019).
- ¹¹W. Li, "High order spectral difference lattice Boltzmann method for incompressible hydrodynamics," *J. Comput. Phys.* **345**, 618–636 (2017).
- ¹²C. Ma, J. Wu, and T. Zhang, "A high order spectral difference-based phase field lattice Boltzmann method for incompressible two-phase flows," *Phys. Fluids* **32**, 122113 (2020).
- ¹³M. Stiebler, J. Tölke, and M. Krafczyk, "An upwind discretization scheme for the finite volume lattice Boltzmann method," *Comput. Fluids* **35**, 814–819 (2006).
- ¹⁴W. Li and L.-S. Luo, "Finite volume lattice Boltzmann method for nearly incompressible flows on arbitrary unstructured meshes," *Commun. Comput. Phys.* **20**, 301–324 (2016).
- ¹⁵Z. Zhao, M. Wen, and W. Li, "A coupled gas-kinetic BGK scheme for the finite volume lattice Boltzmann method for nearly incompressible thermal flows," *Int. J. Heat Mass Transfer* **164**, 120584 (2021).
- ¹⁶M. Zhong, Z. Sen, D. Pan, C. Zhuo, and C. Zhong, "A simplified discrete unified gas kinetic scheme for compressible flow," *Phys. Fluids* **33**, 036103 (2021).
- ¹⁷P. Wang, L. Zhu, Z. Guo, and K. Xu, "A comparative study of LBE and DUGKS methods for nearly incompressible flows," *Commun. Comput. Phys.* **17**, 657–681 (2015).
- ¹⁸H.-B. Luan, H. Xu, L. Chen, Y.-L. Feng, Y. He, and W.-Q. Tao, "Coupling of finite volume method and thermal lattice Boltzmann method and its application to natural convection," *Int. J. Numer. Methods Fluids* **70**, 200–221 (2012).
- ¹⁹Y. Sun and X. Zhang, "A hybrid strategy of lattice Boltzmann method and finite volume method for combined conduction and radiation in irregular geometry," *Int. J. Heat Mass Transfer* **121**, 1039–1054 (2018).
- ²⁰L. Chen, Y.-L. He, Q. Kang, and W.-Q. Tao, "Coupled numerical approach combining finite volume and lattice Boltzmann methods for multi-scale multi-physicscochemical processes," *J. Comput. Phys.* **255**, 83–105 (2013).
- ²¹M. R. Salimi, M. T. Rahni, and F. Jam, "Pore-scale simulation of fluid flow passing over a porously covered square cylinder located at the middle of a channel, using a hybrid MRT-LBM-FVM approach," *Theor. Comp. Fluid Dyn.* **29**, 171–191 (2015).
- ²²Z.-X. Tong and Y.-L. He, "A unified coupling scheme between lattice Boltzmann method and finite volume method for unsteady fluid flow and heat transfer," *Int. J. Heat Mass Transfer* **80**, 812–824 (2015).
- ²³Z.-X. Tong, M.-J. Li, Y.-L. He, and Y.-S. Li, "Numerical Simulation of the particle deposition on a tube with coupled lattice Boltzmann method and finite volume method," *Energy Procedia* **75**, 3207–3212 (2015).
- ²⁴Z.-X. Tong, M.-J. Li, Y.-L. He, and H.-Z. Tan, "Simulation of real time particle deposition and removal processes on tubes by coupled numerical method," *Appl. Energy* **185**, 2181–2193 (2017).
- ²⁵G. D. Ilio, D. Chiappini, S. Ubertini, G. Bella, and S. Succi, "Fluid flow around NACA 0012 airfoil at low-Reynolds numbers with hybrid lattice Boltzmann method," *Comput. Fluids* **166**, 200–208 (2018).
- ²⁶G. D. Ilio, D. Chiappini, S. Ubertini, G. Bella, and S. Succi, "A moving-grid approach for fluid-structure interaction problems with hybrid lattice Boltzmann method," *Comput. Phys. Commun.* **234**, 137–145 (2019).
- ²⁷P. Albuquerque, D. Alemani, B. Chopard, and P. Leone, "Coupling a lattice Boltzmann and a finite difference scheme," in International Conference on Computational Science, Kraków, Poland (2004).
- ²⁸H. B. Luan, H. Xu, L. Chen, D. L. Sun, and W. Q. Tao, "Numerical illustrations of the coupling between the lattice Boltzmann method and finite-type macro-numerical methods," *Numer. Heat Transfer* **57**, 147–171 (2010).
- ²⁹M. Astorino, F. Chouly, and A. Quarteroni, "A time-parallel framework for coupling finite element and lattice Boltzmann methods," *Appl. Math. Res. eXpress* **2016**, 24–67.
- ³⁰Z. Li, M. Yang, and Y. Zhang, "A coupled lattice Boltzmann and finite volume method for natural convection simulation," *Int. J. Heat Mass Transfer* **70**, 864–874 (2014).
- ³¹Z.-X. Tong, M.-J. Li, Y.-L. He, and W.-Q. Tao, "Analysis and numerical tests of lifting relations to reconstruct LBM distribution functions for coupling simulations," *Int. J. Heat Mass Transfer* **107**, 945–955 (2017).
- ³²W.-Q. Tao, *Numerical Heat Transfer* (Xi'an Jiaotong University Press, Xi'an, 2001).
- ³³Z. Guo, B. Shi, and C. Zheng, "A coupled lattice BGK model for the Boussinesq equations," *Int. J. Numer. Methods Fluids* **39**, 325–342 (2002).
- ³⁴G. D. Ilio, D. Chiappini, S. Ubertini, G. Bella, and S. Succi, "Hybrid lattice Boltzmann method on overlapping grids," *Phys. Rev. E* **95**, 013309 (2017).
- ³⁵J. T. Horstmann, T. L. Garrec, D.-C. Mincu, and E. Lévéque, "Hybrid simulation combining two space-time discretization of the discrete-velocity Boltzmann equation," *J. Comput. Phys.* **349**, 399–414 (2017).
- ³⁶X. He, X. Shan, and G. D. Doolen, "Discrete Boltzmann equation model for nonideal gases," *Phys. Rev. E* **57**, R13–R16 (1998).
- ³⁷X. He, S. Chen, and G. D. Doolen, "A novel thermal model for the lattice Boltzmann method in incompressible limit," *J. Comput. Phys.* **146**, 282–300 (1998).
- ³⁸T. Lee and C.-L. Lin, "An Eulerian description of the streaming process in the lattice Boltzmann equation," *J. Comput. Phys.* **185**, 445–471 (2003).
- ³⁹A. Fakhari, M. Geier, and T. Lee, "A mass-conserving lattice Boltzmann method with dynamic grid refinement for immiscible two-phase flows," *J. Comput. Phys.* **315**, 434–457 (2016).
- ⁴⁰L. Kovasznay, "Laminar flow behind a two-dimensional grid," *Math. Proc. Cambridge Philos. Soc.* **44**, 58–62 (1948).
- ⁴¹U. Ghia, K. N. Ghia, and C. T. Shin, "High-Re solutions for incompressible flow using the Navier-Stokes equations and a multigrid method," *J. Comput. Phys.* **48**, 387–411 (1982).
- ⁴²S. P. Vanka, "Block-implicit multigrid solution of Navier-Stokes equation in primitive variables," *J. Comput. Phys.* **65**, 138 (1986).

- ⁴³S. Hou, Q. Zou, S. Chen, G. Doolen, and A. C. Cogley, "Simulation of cavity flow by the lattice Boltzmann method," *J. Comput. Phys.* **118**, 329–347 (1995).
- ⁴⁴L.-S. Luo, W. Liao, X. Chen, Y. Peng, and W. Zhang, "Numerics of the lattice Boltzmann method: Effects of collision models on the lattice Boltzmann simulations," *Phys. Rev. E* **83**, 056710 (2011).
- ⁴⁵D. J. Tritton, "Experiments on the flow past a circular cylinder at low Reynolds numbers," *J. Fluid. Mech.* **6**, 547–567 (1959).
- ⁴⁶M. Coutanceau and R. Bouard, "Experimental determination of the main features of the viscous flow in the wake of a circular cylinder in uniform translation. I—Steady flow," *J. Fluid. Mech.* **79**, 231–256 (1977).
- ⁴⁷X. He and G. Doolen, "Lattice Boltzmann method on curvilinear coordinates system: Flow around a circular cylinder," *J. Comput. Phys.* **134**, 306–315 (1997).
- ⁴⁸K. Hejranfar and E. Ezzatneshan, "Implementation of a high-order compact finite-difference lattice Boltzmann method in generalized curvilinear coordinates," *J. Comput. Phys.* **267**, 28–49 (2014).
- ⁴⁹D. Hartmann, M. Meinke, and W. Schröder, "A strictly conservative Cartesian cut-cell method for compressible viscous flows on adaptive grids," *Comput. Methods Appl. Mech. Eng.* **200**, 1038–1052 (2011).
- ⁵⁰H. J. Kim and P. A. Durbin, "Observations of the frequencies in a sphere wake and of drag increase by acoustic excitation," *Phys. Fluids* **31**, 3260–3265 (1988).